TITLE

Active zone compaction in presynaptic homeostatic potentiation

AUTHORS

Achmed Mrestani[1], Philip Kollmannsberger[2], Martin Pauli[1,6], Felix Repp[1,2,6], Robert J. Kittel[1,3,4], Jens Eilers[4], Sören Doose[5], Markus Sauer[5], Anna-Leena Sirén[6], Manfred Heckmann[1*], Mila M. Paul[1*]

[1] Institute for Physiology, Department of Neurophysiology, Julius-Maximilians-University Würzburg, D-97070 Würzburg, Germany

[2] Center for Computational and Theoretical Biology, Julius-Maximilians-University Würzburg, D-97074 Würzburg, Germany

[3] Institute of Biology, Department of Animal Physiology, Leipzig University, D-04103 Leipzig, Germany

[4] Carl-Ludwig-Insitute for Physiology, Leipzig University, D-04103 Leipzig, Germany

[5] Department of Biotechnology and Biophysics, Julius-Maximilians-University Würzburg, D-97074 Würzburg, Germany

[6] Department of Neurosurgery, University Hospital of Würzburg, D-97080 Würzburg, Germany

[*] Correspondence should be adressed to M.H. (heckmann@uni-wuerzburg.de) and M.M.P. (mila.paul@uni-wuerzburg.de)

CLASSIFICATION

major category: Biological Sciences, minor category: Neuroscience

KEYWORDS

active zone, Bruchpilot, compaction, homeostasis, presynaptic plasticity, super-resolution microscopy

AUTHOR CONTRIBUTIONS

A.M., J.E., A.L.S., M.S., M.H. and M.M.P designed experiments. A.M., M.P., M.H. and M.M.P. performed experiments. A.M., P.K., F.R., M.P., R.J.K., J.E., S.D., M.H. and M.M.P analyzed the data. A.M., M.H. and M.M.P. wrote the manuscript with the help

of all co-authors. A.L.S., M.S., M.H. and M.M.P. coordinated the study and provided funding.

This PDF file includes:

Main Text

Figures 1-5

Supplementary Figures 1-5

Supplementary Table 1

ABSTRACT

Brain function relies on neurotransmission which is stabilized by presynaptic homeostatic potentiation (PHP). PHP operates on time scales ranging from minute- to life-long adaptations and likely involves reorganization of presynaptic active zones (AZs). At *Drosophila melanogaster* neuromuscular junctions, earlier work ascribed AZ enlargement by incorporating more Bruchpilot (Brp) scaffold protein a central mechanistic role in PHP.

We used localization microscopy (*direct* stochastic optical reconstruction microscopy, *d*STORM) and hierarchical density-based spatial clustering of applications with noise (HDBSCAN) to study AZ plasticity during PHP. We found that both acute, philanthotoxin (PhTx)-induced and chronic, genetically-induced PHP lead to compaction of individual AZs without altering Brp copy numbers per AZ. This compaction even occurs within Brp subclusters of the AZ scaffold which also move towards AZ centers. Furthermore, lowering imaging resolution revealed how AZ compaction in PHP translates into apparent increases in AZ area and Brp protein content as implied earlier. Our results suggest AZ compaction in PHP as an effective mechanism to raise presynaptic protein density and transmitter release.

SIGNIFICANCE STATEMENT

Homeostatic plasticity stabilizes chemical synaptic transmission in multiple organisms ranging from insects to humans. Changes in active zones (AZs), membrane specializations of the presynapse where synaptic vesicles are discharged, are thought to be crucial in homeostatic adaptations. AZ growth by protein incorporation was proposed as a core mechanism in presynaptic homeostatic potentiation (PHP). Localization microscopy of an abundant AZ scaffold protein uncovered that instead of

growing, AZs are compacted in acute and chronic PHP. At lower imaging resolution, however, AZs appear larger and brighter although protein numbers are not increased. In summary, our findings suggest AZ compaction as new and effective mechanism to raise presynaptic protein density and transmitter release in PHP.

INTRODUCTION

Chemical synapses are complex nanomachines that integrate and process information. Synapses are optimized for fast and reliable performance in combination with miniaturization and plasticity (Atwood and Karunanithi, 2002; Chua et al., 2010; Kittel and Heckmann, 2016; Neher and Brose, 2018). An intriguing form of synaptic plasticity is presynaptic homeostatic potentiation (PHP, Turrigiano, 2008; Davis and Müller, 2015). Homeostatic plasticity has been studied at vertebrate synapses (Turrigiano et al., 1998; Murthy et al., 2001; Thiagarajan et al., 2005; Lindskog et al., 2010; Jeans et al., 2017; Delvendahl et al., 2019) as well as at *Drosophila melanogaster* neuromuscular junctions (NMJs, Davis and Goodman, 1998; DiAntonio et al., 1999; Frank et al., 2006; Müller et al., 2012; Younger et al., 2013; Orr et al., 2017; Gratz et al., 2019). While the structural correlates of PHP remain elusive, several mechanisms are conceivable including incorporation, removal, modification and/or rearrangement of key proteins at active zones (AZs), presynaptic membrane specializations where synaptic vesicles are discharged.

The cytomatrix at the active zone (CAZ) consists of an organized set of proteins (Südhof 2012). Large α-helical coiled-coil proteins of the ELKS/CAST family are crucial for the regulation of synaptic transmission (Held et al., 2016; Dong et al., 2018). In *Drosophila,* the ELKS/CAST homolog Bruchpilot (Brp) is essential for synchronous glutamate release and its amount was shown to correlate with release probability and structural synaptic differentiation (Kittel et al., 2006; Ehmann et al., 2014; Peled et al., 2014; Paul et al., 2015; Akbergenova et al., 2018). Brp is a major AZ scaffold protein responsible for clustering of presynaptic calcium channels close to release sites creating a proper molecular environment for fast and precise neurotransmitter release (Kittel et al., 2006; Held and Kaeser, 2018). Whereas the Brp N-term was mapped in membrane-proximity, its C-term localizes about 155 nm above the postsynaptic receptors (Fouquet et al., 2009; Liu et al., 2011) and is important for tethering synaptic vesicles (Hallermann et al., 2010). Remarkably, Brp is distributed heterogeneously at *Drosophila* NMJs forming about 15 subclusters within an AZ (Ehmann et al., 2014). Subclusters with high protein concentration should promote vesicle tethering as shown for Syntaxin (Sieber et al., 2007; Barg et al., 2010; van den Bogaart et al., 2011). Early work at *Drosophila* NMJs showed no evidence for protein synthesis during PHP (Frank et al., 2006). However, confocal and STED microscopy suggested an increase in Brp

amount during acute and chronic PHP (Weyhersmüller et al., 2011; Goel et al., 2017; Böhme et al., 2019).

Here, we reason that localization microscopy in terms of *direct* stochastic optical reconstruction microscopy (*d*STORM, Heilemann et al., 2008; van de Linde et al., 2011; Löschberger et al., 2012) permits precise quantification of Brp in PHP (Ehmann et al., 2014; Paul et al., 2015). For unbiased data analysis we perform hierarchical density-based spatial clustering of applications with noise (HDBSCAN, Campello et al., 2013). We address the following fundamental questions: How robust are localization-based results relying on density-based clustering algorithms? Does the amount of protein within individual AZs increase during PHP and/or does the nanoarchitecture of the AZ scaffold change? Do AZs grow or shrink? Using data simulations and correlative confocal–*d*STORM imaging we analyze the relation between thresholding- and localization-based fluorescence quantification of small structures below the diffraction limit. We discover striking differences of Brp organization during acute, pharmacologically-induced and chronic, genetically-induced homeostasis and reason that AZ compaction and not AZ growth is the structural correlate of release strengthening in PHP.

RESULTS

Analysis of super-resolution data

We imaged type Ib boutons on abdominal muscles 6 and 7 of male *Drosophila melanogaster* 3rd instar larvae (Figure 1A) using *d*STORM (Heilemann et al., 2008; van de Linde et al., 2011; Löschberger et al., 2012; Ehmann et al., 2014; Paul et al., 2015) and a highly specific monoclonal antibody Brp^{Nc82}, that maps to the C-terminal region of Brp (Kittel et al., 2006; Fouquet et al., 2009). Since Brp is an abundant protein and our epitope in Brp covers the spatial extent of individual AZs, we interpret 'Brp area' as 'AZ area'. Density-based clustering algorithms allow to study synaptic nanotopology (Bar-On et al., 2012; Ehmann et al., 2014; Szoboszlay et al., 2017; Rahbek-Clemmensen et al., 2017; Rebola et al., 2019). We used a Python implementation of hierarchical density-based spatial clustering of applications with noise (HDBSCAN), which robustly extracts clusters in data with varying density (Campello et al., 2013; McInnes et al., 2017). To test the algorithm's robustness, we varied its free parameters 'minimum cluster size' and 'minimum samples' and analyzed their influence on the number of detected Brp clusters, the number of Brp localizations and the area per cluster (Figure 1B-E, Supplementary Figure 1). A wide range of parameters delivered robust results and all Brp clusters in the following analyses were extracted with the combination 100 and 25 for minimum cluster size and minimum samples, respectively.

To probe the existence of Brp subclusters in our data we computed H functions (derivative of Ripley's K function) and calculated an averaged curve (Figure 1F). Positive values for H(r) indicate clustering, negative dispersion or edge effects, and maximum positive values roughly correspond to the radius of putative clusters (Kiskowski et al., 2009). The maximum of the curve at 22 nm is in agreement with the dimensions of Brp subclusters reported in earlier work (Ehmann et al., 2014). Subsequently, we performed a second HDBSCAN on individual AZs with adjusted parameters that yielded similar subcluster radii as the H function (Figure 1G, H). In addition to alpha shape generation for area determination, localization-based analysis yields the possibility to define a center of mass (c.o.m.) of an individual subcluster and of the entire AZ and to measure their specific interspaces (Figure 1G). The distance between AZ c.o.m. and subcluster c.o.m. will be referred to as radial distance.

Compaction of the Bruchpilot scaffold in acute and chronic homeostasis

161 The wasp venom Philanthotoxin (PhTx) induces PHP within minutes and increases
162 quantal content and release-ready vesicles in our preparation (Frank et al., 2006;
163 Weyhersmüller et al., 2011; Davis and Müller, 2015). We compared AZs of type Ib
164 boutons incubated in PhTx (phtx) or DMSO (control, Figure 2A). Brp localization
165 numbers as a measure for the amount of Brp protein per AZ (Ehmann et al., 2014)
166 were not changed in phtx, however, AZ area was reduced compared to controls and,
167 hence, Brp density increased in phtx (Figure 2B, see Supplementary Table 1 for all
168 data presented here). Thus, PHP induces a rearrangement of Brp without changing
169 the number of Brp molecules within individual AZs of type Ib boutons.
170 Previous work discovered a proximo-distal functional and structural gradient with distal
171 type Ib boutons containing more AZs, more Brp per AZ and releasing more glutamate
172 than proximal boutons (Peled and Isacoff, 2011; Ehmann et al., 2014; Paul et al.,
173 2015). To test whether the above described changes in phtx occur in a distinct spatial
174 pattern within the NMJ we performed a subgroup analysis of AZs in boutons number
175 1-6 (Paul et al., 2015). Spearman correlation coefficients displayed no correlation
176 between bouton number and Brp localization density in both groups (Supplementary
177 Figure 2A). Thus, structural plasticity in acute homeostasis appears to occur
178 homogeneously within the NMJ. Furthermore, there was neither a change in the total
179 number of localizations nor the amount of unclustered Brp localizations outside AZs
180 per bouton (Supplementary Figure 2B).
181 To clarify whether AZ compaction only appears after an acute homeostatic challenge
182 or whether it is a general phenomenon in PHP, we used a knockout of the postsynaptic
183 glutamate receptor subunit GluRIIA as a genetic, 'chronic' PHP model (GluRIIAko,
184 Petersen et al., 1997; DiAntonio et al., 1999; Frank et al., 2006). We performed
185 *d*STORM imaging and HDBSCAN analysis in GluRIIAko and wildtype larvae as
186 described before (Figure 2C). Remarkably, we found comparable effects to PhTx
187 treatment with unchanged Brp localization numbers per AZ, decreased AZ area and
188 higher Brp density (Figure 2D). Thus, Brp scaffolds are also compacted in chronic PHP.
189
190 **AZ subcluster compaction**
191 Next, we tested whether AZ reorganization during PHP also takes place within AZ
192 subclusters (Figure 3A, C). Brp subcluster number per AZ was unchanged in phtx and
193 GluRIIAko versus controls (Figure 3B, D). While Brp localization numbers in
194 subclusters were unchanged, subcluster area was decreased (Figure 3B, D). Thus,

195 mean Brp localization density in subclusters increased in acute and chronic PHP
196 (Figure 3B, D). We also examined the radial distances between the c.o.m. of an
197 individual AZ and the c.o.m.s of its subclusters and found that they decreased in phtx
198 and GluRIIAko compared to controls (Figure 3B, D). In addition, the minimum distance
199 between subcluster c.o.m.s was decreased in both forms of PHP, whereas the space
200 between subclusters was only reduced in chronic PHP (Supplementary Figure 5).
201 Taken together, these data show that Brp is compacted within AZ subclusters in acute
202 and chronic homeostasis but the number of Brp molecules does not increase.
203 Next, we quantified the circularity of Brp clusters as the ratio of their Eigenvalues of
204 the covariance matrix (ratio between 0 and 1 with 1 indicating a perfect circle, i.e.
205 presumably in top view, see Material and Methods). AZ circularity was similar in phtx
206 and control, thus, analysis of the entire dataset without orientation selection appears
207 appropriate. We then investigated the relation between AZ area and circularity.
208 Interestingly, this uncovered an inverse correlation (Supplementary Figure 2C). We
209 interpret that low circularity is indicative of AZs in side view or of large Brp spots that
210 partially arise from merged AZs lying nearby in 2D projection. The latter have been
211 referred to as double ring structures, grouped CAZ units, or cluster AZs (Kittel et al.,
212 2006; Ehmann et al., 2014; Akbergenova et al., 2018). Assuming that some structural
213 parameters depend strongly on AZ orientation, we analyzed AZ area and radial
214 distance in a subsample of AZs with circularity ≥ 0.5 and more planar orientation
215 (Supplementary Figure 2D). Again, we found a pronounced decrease in AZ area and
216 a similar decrease of radial distance in both groups. This indicates that AZ compaction
217 in PHP appears regardless of AZ orientation.
218 In earlier studies abdominal muscle 4 which exclusively forms type Ib boutons was
219 used to analyze structural effects of PhTx on AZs (Goel et al., 2017; Böhme et al.,
220 2019). Therefore, we imaged PhTx treated AZs on abdominal muscle 4 and applied
221 the described cluster analysis. This yielded similar results as shown for AZs on
222 abdominal muscles 6/7 including subcluster parameters (Supplementary Figure 3).
223
224 **Correlative confocal-*d*STORM imaging of AZs**
225 Earlier confocal and STED microscopy reported an increased fluorescence intensity in
226 PHP and interpreted this as evidence for protein recruitment to the AZ (Weyhersmüller
227 et al., 2011; Goel et al., 2017; Böhme et al., 2019). Since our results are in sharp
228 contrast to these findings we wondered whether the difference in molecular density

229 before and after PHP could bias AZ area quantification either in our localization-based
230 approach or in intensity-based approaches (confocal and STED microscopy). To test
231 this, we compared both methods using simulated circular clusters without noise and
232 subclustering (Supplementary Figure 4). Our results indicate that the area of large
233 objects with low molecular density (i.e. lower fluorescence intensity) can be grossly
234 misjudged by pixel- and intensity-based quantification, which could explain the
235 discrepancy between our and earlier findings. To further examine this experimentally,
236 we perfomed sequential confocal-*d*STORM imaging of Brp in type Ib boutons (Figure
237 4A, B). Confocal data were analyzed with an intensity threshold of 100 a. u. (Figure
238 4Aii). Figure 4C shows enlarged AZs overlaid in confocal and *d*STORM resolution from
239 Figure 4A and B in green, magenta and blue to mark AZ identity. The examples
240 demonstrate area overestimation due to high localization density (Figure 4Ci) and
241 show that on the other hand thresholding of confocal images can lead to complete loss
242 of signal that is included in *d*STORM quantification (Figure 4Cii). Additionally,
243 segmentation of closely spaced AZs is clearly superior using HDBSCAN-based
244 quantification of localization data compared to thresholding-based quantification of
245 confocal data (Figure 4Ciii). In a next step, we quantified AZs in the complete dataset
246 after correlative confocal-*d*STORM imaging. Distribution of AZ area was broader in
247 confocal microscopy than in *d*STORM (Figure 4D). As expected, we obtained positive
248 correlations between the localization density per AZ measured with *d*STORM and the
249 mean pixel intensity per AZ measured with confocal (Figure 4E). Interestingly,
250 localization density correlated stronger with confocally measured than *d*STORM-
251 measured AZ area (Figure 4F) matching our simulation results (Supplementary Figure
252 4). Confocal microscopy mostly overestimates AZ area, whereas underestimation only
253 occurs at low AZ localization density (Figure 4G). This indicates that higher localization
254 density in *d*STORM leads to an apparent enlargement of AZ area reported by
255 thresholded confocal microscopy.
256
257 **Homeostatic compaction is translated into an apparent area increase**
258 In contrast to earlier studies (Weyhersmüller et al., 2011; Goel et al., 2017; Böhme et
259 al., 2019) we found smaller AZ areas but increased localization density following PHP.
260 To gain a better understanding of this discrepancy we performed simulations of
261 confocal spatial resolution applying a Gaussian filter of 150 nm SD (Figure 5A, B). 3D
262 histograms of two example AZs in control and phtx illustrate the applied thresholding

(Figure 5C, compare Figure 4B in Weyhersmüller et al., 2011). In phtx, AZ area is decreased and localization density increased in original *d*STORM resolution (x-axes, Figure 5D, E), whereas both AZ area and mean pixel intensity increased in the same images in simulated confocal resolution (y-axes). We conclude that intensity-based quantification with confocal resolution may lead to inverse results concerning AZ area compared to localization-based analysis. In a last step, we simulated STED resolution as a less dramatic resolution decrease applying a Gaussian filter of 25 nm SD (Figure 5F). AZ area was measured similarly as mentioned above, AZ diameter was estimated from AZ area and intensity maxima per AZ were detected in selected planar-oriented AZs with a peak finding algorithm in FIJI after thresholding (Material and Methods; Böhme et al., 2019). This indicated an increase in AZ area, AZ diameter and number of intensity maxima per AZ after induction of PHP (Figure 5G), apparent findings contrary to our localization-based data evaluation. In summary, simulation of lower resolution gives inverse results for the number of clusters per AZ matching aforementioned findings.

DISCUSSION

We introduce AZ compaction as a mechanism for presynaptic structural adaptation in acute and chronic PHP. Compaction encompasses reduced AZ area and enhanced molecular density without increasing protein amount. Brp subclusters are likewise compacted and located closer to AZ centers during PHP. Notably, AZ compaction appears as an increase of AZ area in thresholding-based analysis, explaining the apparent contradiction with earlier results.

Protein proximity promotes vesicle traffic

Despite substantial progress in single-molecule based microscopy, resolving the spatial relations between individual subcellular molecules remains challenging (Nahmani et al., 2017). In this study, we reason that *d*STORM and a localization-based clustering algorithm are a powerful experimental conjunction to decipher protein dense networks at single presynaptic AZs. The effects reported here are small in absolute terms, but very reproducible under different conditions (Figure 2 and 3, Supplementary Figure 2, 3 and 5). In the light of mechanistic considerations, it is plausible that changes of molecular proximities at AZs in the nanometer range lead to considerable functional consequences (Neher 1998). For example, it is established for the t-SNARE protein Syntaxin that the formation of protein clusters enhances local protein concentration, which in turn may raise the probability of protein interactions (Sieber et al., 2007; van den Bogaart et al., 2011). Furthermore, in hippocampal neurons RIM clusters with diameters of ~80 nm were described to show remarkable reorganization during synaptic plasticity (Tang et al., 2016). Molecular concentrations can be estimated from our data and Brp molecule numbers per AZ reported previously by Ehmann et al., 2014 assuming a distribution of the Brp^{Nc82} epitope in a hemisphere. For radii of 185 and 175 nm (Figure 2D, Supplementary Table 1) the hemisphere volumes before and after PHP are ~0.013 and 0.011 μm^3. 170 Brp molecules (Ehmann et al., 2014) yield concentrations of 21 and 25 µM before and after PHP, respectively. Thus, the ~7 % density increase translates into a 19 % concentration increase. Brp subclusters are assumed to contain bundles of ~7 Brp molecules creating a platform for a single synaptic vesicle as described below (Ehmann et al., 2014). For hemispheres with subcluster radii of 22.5 and 21.7 nm (Figure 3D) this yields protein concentrations of 490 and 540 µM before and after PHP. While the above-mentioned estimates for Brp concentrations in the whole AZ are probably reasonably accurate, the estimates for

313 the concentration in subclusters provide only a lower limit. Here, subcluster radii are
314 most certainly overestimated due to the linkage error introduced by the combination of
315 a primary antibody with the secondary $F(ab')_2$ fragment leading to a 'labeling complex
316 diameter' of 26 nm (Ehmann et al., 2014). Thus, local protein concentrations could be
317 even higher and, likewise, the difference in the two scenarios. This could be clarified
318 in future studies using smaller labeling approaches, e.g. directly fluorophore-
319 conjugated Brp^{Nc82} $F(ab')_2$ fragments. Brp was shown to directly or indirectly tether
320 synaptic vesicles at AZs via its C-term (Hallermann et al., 2010; Scholz et al., 2019).
321 Other coiled-coil proteins like Golgins tether and traffic vesicles at the Golgi network
322 by guidance via multiple vesicle-binding sites (Gillingham and Munro, 2016; Cheung
323 and Pfeffer, 2016). Likewise, Brp could provide a meshwork guiding vesicles via
324 multiple vesicle-interaction sites represented by subclusters. The Brp^{Nc82} epitope is
325 located close to the C-term and an increased protein concentration, achieved by AZ
326 compaction, could enhance the probability of these interactions and facilitate vesicle
327 supply. Taking the ~40.5 nm vesicle diameter from Karunanithi et al., 2002 and adding
328 ~10 nm of protein trimmings (Takamori et al., 2006) resulting in 50-60 nm veritable
329 vesicle extent, the distance between Brp clusters should fit approximately these
330 dimensions. This is the case and since we observe compaction of Brp subclusters and
331 a reduced radial distance this should further enhance trafficking of vesicles over the
332 surface generated by Brp C-terms (Supplementary Figure 5). This structural adaption
333 is in line with evidence for increased vesicle traffic during PHP (Weyhersmüller et al.,
334 2011; Delvendahl et al., 2019).
335
336 Vesicle cluster formation depends on liquid-liquid phase separation, achieved by
337 intrinsically disordered regions (IDRs, Milovanovic et al., 2018). Glutamine-rich IDRs
338 were implicated in the formation of coiled-coils and protein agglomerates (Fiumara et
339 al., 2010). The vesicle tethering Brp C-term comprises a stretch of glutamine residues
340 (Hallermann et al., 2010). Vesicle traffic in liquid-liquid phase separation with Brp C-
341 terms could profit from AZ compaction. While the molecular binding partners of the Brp
342 C-term are still unclear, a functional interaction with Complexin was reported (Scholz
343 et al., 2019). We assume that all Brp molecules forming one subcluster create a
344 platform for tethering a single synaptic vesicle. This hypothesis matches reasonably
345 well with EM studies describing on average 12 vesicles tethered to a single CAZ

346 (Böhme et al., 2016) and with reconstructions of EM tomography data (Zhan et al.,
347 2016).
348
349 **Compaction of the AZ scaffold without recruitment of Brp molecules**
350 Localization data can be used to estimate protein numbers (Ehmann et al., 2014;
351 Löschberger et al., 2012). In this study, the number of Brp localizations (i.e. Brp
352 molecules) did not change after induction of homeostasis, which is in line with previous
353 work ruling out protein synthesis during PHP (Frank et al., 2006). Confocal and STED
354 microscopy provided data which were interpreted as evidence for protein incorporation
355 into AZs during acute and chronic homeostasis (Weyhersmüller et al., 2011; Goel et
356 al., 2017; Böhme et al., 2019). However, our data support an alternative interpretation
357 (Figure 2B, D, Supplementary Figure 2B). Confocal and STED data were analyzed
358 using pixel- and thresholding-based approaches that depend on signal intensity
359 (Weyhersmüller et al., 2011; Goel et al., 2017; Böhme et al., 2019). Here, we show
360 that large structures with low intensity appear smaller than small structures with higher
361 intensity (Supplementary Figure 4C). We performed correlative confocal-*d*STORM
362 imaging and demonstrated that a higher protein density in *d*STORM translates into an
363 apparent area increase in confocal microscopy (Figure 4F). In confocal microscopy
364 usually a stack of multiple slices is obtained, whereas in 2D-*d*STORM we sampled only
365 signal from a single focal plane. However, we found no evidence for signal that is
366 included in confocal images but is missing in corresponding *d*STORM data (compare
367 Figure 4Ai and B). We measured that the z-range of boutons in confocal stacks ranges
368 from 800 nm to 2 µm, roughly corresponding to the axial capture range of our *d*STORM
369 measurements (Tokunaga et al., 2008). The correlation between localization density
370 and AZ area in confocal microscopy is corroborated by simulating confocal resolution
371 (Figure 5D, E).
372
373 **A molecular concept of homeostatic plasticity**
374 Diverse cellular plasticity mechanisms enable the remarkable capacity of the nervous
375 system to adapt, refine and increase in strength. Among them, the unique form of
376 homeostatic plasticity stabilizes brain function on time scales of minutes to decades
377 proceeding via different molecular pathways (Turrigiano et al., 2008; Younger et al.,
378 2013; Orr et al., 2017; Ortega et al., 2018; Frank et al., 2020). We here report that
379 compaction of the AZ scaffold is a crucial hallmark of homeostasis, due to the increase

380 of protein density and therefore promotion of vesicle traffic. In contrast, disuse
381 hypersensitivity, another form of synaptic plasticity induced by blockade of the AMPA
382 glutamate receptor, was linked to AZ enlargement reversable by application of PhTx
383 (Murthy et al., 2001; Thiagarajan et al., 2005). This illustrates that distinct forms of
384 plasticity can exhibit varying structural expressions. At the *Drosophila* NMJ a proximo-
385 distal gradient in release strength is accompanied by (ultra-)structural adaptations of
386 AZs (Peled and Isacoff, 2011; Ehmann et al., 2014; Paul et al., 2015). To test whether
387 this form of intraneuronal differentiation influences the ability of an AZ to undergo
388 homeostatic plasticity, we analyzed our *d*STORM data according to this aspect.
389 Interestingly, we find that PHP increases Brp density regardless of the bouton position
390 (Supplementary Figure 2A).
391
392 We describe compaction on the level of individual AZs (i.e. clusters of Brp epitopes)
393 and of Brp subclusters. However, the molecular mechanism of compaction for release
394 strengthening might be extended to other AZ molecules. Orr et al., 2017 demonstrated
395 that the Semaphorin2b-PlexinB complex regulates PHP via control of presynaptic
396 actin. Whereas the role of actin for synaptic efficacy has been described
397 unambiguously (Cingolani and Goda, 2008), the significance for compaction of AZs
398 remains to be determined. Furthermore, AZ molecules located in membrane-proximity
399 like ENaCs (Younger et al., 2013), presynaptic calcium channels (Turrigiano 2008),
400 RIM and RIM-binding protein should be examined using superresolution microscopy
401 to determine whether compaction is a universal plasticity concept during PHP. Finally,
402 it appears promising to correlate transmission properties of individual AZs with its
403 nanoarchitecture using transgenically expressed GCaMP Ca^{2+} sensors (Akbergenova
404 et al., 2018; Gratz et al., 2019) to link synaptic activity with ultrastructure.
405

406 **MATERIAL AND METHODS**
407
408 **Fly stocks**
409 Flies were raised on standard cornmeal and molasses medium at 25 °C. *Drosophila*
410 *melanogaster* male 3rd instar larvae of the following strains were used for experiments:
411 Wildtype: w^{1118} (Bloomington *Drosophila* Stock Center). GluRIIA knockout:
412 $DGluRIIA^{AD9}/Df(2L)cl^{h4}$ (kindly provided by Mathias A. Böhme).
413
414 **Philanthotoxin treatment and and larval preparation**
415 Philanthotoxin 433 tris (trifluoroacetate) salt (PhTx, P207 Sigma) was dissolved in
416 dimethyl sulfoxide (DMSO) to obtain a stock solution of 4 mM and stored at -20 °C. For
417 each experiment, the respective volume was further diluted with freshly prepared
418 haemolymph-like solution (HL-3, Stewart et al., 1994) to a final PhTx concentration of
419 20 µM in 0.5 % DMSO. Control experiments were performed with the same DMSO
420 concentration in HL-3. PhTx treatment of semi-intact preparations was performed
421 essentially as described previously (Frank et al., 2006). In brief, larvae were pinned
422 down in calcium-free, ice-cold HL-3 at the anterior and posterior endings, followed by
423 a dorsal incision along the longitudinal axis. Larvae were incubated in 10 µl of 20 µM
424 PhTx in DMSO for 10 minutes at room temperature (22 °C). Following this incubation
425 time, PhTx was replaced by HL-3 and larval preparations were completed, followed by
426 fixation and staining.
427
428 **Fixation, staining and immunofluorescence**
429 After PhTx treatment and dissection, larvae were fixed with 4 % paraformaldehyde in
430 phosphate buffered saline (PBS) for 10 minutes and blocked for 30 minutes with PBT
431 (PBS containing 0.05 % Triton X-100, Sigma) including 5 % natural goat serum
432 (Dianova). Primary antibodies were added for overnight staining at 4 °C. After two short
433 and three long (20 min each) washing steps with PBT, preparations were incubated
434 with secondary antibodies for 3 hours at room temperature, followed by two short and
435 three long washing steps with PBT. Preparations were kept in PBS at 4 °C until
436 imaging. All data were obtained from NMJs formed on abdominal muscles 6/7 in
437 segments A2 and A3, except data for Supplementary Figure 3, which were obtained
438 from NMJs formed on abdominal muscle 4 in segments A2-A4. Directly compared data
439 (e.g. Figure 2B) were obtained from larvae stained in the same vial and measured in
440 one imaging session.

441 ***d*STORM (*direct* stochastic optical reconstruction microscopy)**

442 Super-resolution imaging of the specimen was performed essentially as previously
443 reported (Ehmann et al., 2014; Paul et al., 2015). Preparations were incubated with
444 monoclonal antibody (mAb) Brp^{Nc82} (1:100, Antibody Registry ID: AB_2314866,
445 Developmental Studies Hybridoma Bank) and secondary antibody goat α-mouse
446 $F(ab')_2$ fragments labelled with Alexa Fluor647 (1:500, A21237, Thermofisher).
447 Boutons were visualized using Alexa Fluor488 conjugated goat α-horseradish-
448 peroxidase antibody (α-hrp, 1:250, Jackson Immuno Research). After staining, larval
449 preparations were incubated in 100 mM mercaptoethylamine (MEA, Sigma-Aldrich) in
450 a 0.2 M sodium phosphate buffer, pH 7.8 to 7.9, to allow reversible switching of single
451 fluorophores during data acquisiton (van de Linde et al., 2008). The buffer additionally
452 included an oxygen-scavenging system (10% (wt/vol) glucose, 10 U/ml glucose
453 oxidase and 200 U/ml catalase). In all experiments, images were acquired using an
454 inverted microscope (Olympus IX-71, 60x, NA 1.49, oil immersion) equipped with a
455 nosepiece-stage (IX2-NPS, Olympus). 647 nm (F-04306-113, MBP Communications
456 Inc.) and 488 nm (iBEAM-SMART-488-S, Toptica) lasers were used for excitation of
457 Alexa Fluor647 and Alexa Fluor488, respectively. Laser beams were passed through
458 clean-up filters (BrightLine HC 642/10, Semrock and ZET 488/10, Chroma,
459 respectively), combined by a dichroic mirror (LaserMUX BS 473-491R, 1064R, F38-
460 M03, AHF Analysentechnik), and directed onto the probe by an excitation dichroic
461 mirror (HC Quadband BS R405/488/532/635, F73-832, AHF Analysentechnik). The
462 emitted fluorescence was filtered with a quadband-filter (HC-quadband
463 446/523/600/677, Semrock) and a longpass- (Edge Basic 635, Semrock) or bandpass-
464 filter (Brightline HC 582/75, Semrock) for the red and green channel, respectively, and
465 divided onto two cameras (iXon Ultra DU-897-U, Andor) using a dichroic mirror (HC-
466 BS 640 imaging, Semrock). The green channel was used for visualizing individual
467 presynaptic boutons in normal fluorescence microscopy. For the red channel, image
468 resolution was 126 nm x 126 nm per pixel to obtain super-resolution of Brp. Single
469 fluorophores were localized and high resolution-images were reconstructed with
470 rapi*d*STORM (Heilemann et al., 2008; van de Linde et al., 2011; Wolter et al., 2010;
471 Wolter et al., 2012; www.super-resolution.de). Only fluorescence spots with more than
472 12000 photons were analyzed and subpixel binning of 10 nm px^{-1} was applied. For
473 visualization of representative *d*STORM measurements (Figure 4B, Figure 5A, B, F),
474 reconstructed images from rapi*d*STORM with 5 nm binning were opened in FIJI

475 (Schindelin et al., 2012) and where contrast enhanced for clarity. Localization precision
476 was determined with the NeNa algorithm (nearest neighbor based analysis,
477 Endesfelder et al. 2014), implemented in the LAMA software package (LocAlization
478 Microscopy Analyzer; Malkusch and Heilemann, 2016) in 108 *d*STORM
479 measurements of Brp and was 6.3 ± 0.6 nm (mean ± SD) in this study. To check for
480 homogenous illumination of the samples we analyzed and compared localization
481 intensity of all *d*STORM measurements, (i) for the whole image, and (ii) only for
482 analyzed regions and found no differences in A/D counts between the groups.
483
484 **Confocal microscopy**
485 For confocal imaging larvae were mounted in PBS and imaged using a commercial
486 confocal laser scanning microscope (Zeiss LSM 700) equipped with an oil-immersion
487 objective (Plan-Apochromat 63x/1.40 Oil M27). Alexa Fluor647 and Alexa Fluor488
488 were excited with the 639 nm and the 488 nm diode laser lines, repectively. The
489 microscope was controlled via ZEN 12 software (black edition, Zeiss AG). For each z-
490 stack 7-13 slices with 200 nm axial spacing were obtained. The gain of the
491 photomultiplier tubes was adjusted to 700 and 600 V and laser power was set to 1.5
492 % and 1 % in the red and green channel, respectively, to obtain a good signal with little
493 photobleaching allowing subsequent *d*STORM imaging. The pinhole was set to 70.6
494 µm, corresponding to 1.32 Airy units in the red and 1.73 Airy units in the green channel.
495 Images were recorded in 1024 x 1024 (lines x pixels) format with 16-bit data depth.
496 Given an approximate resolution of 200 nm in the red channel, the pixel size, adjusting
497 the zoom factor to 1.2, was set to about 83 nm for sufficient data sampling. Settings
498 resulted in a pixel dwell time of 3.15 µs.
499
500 **Data evaluation**
501 Localization microscopy data were analyzed with custom written Python code
502 (https://www.python.org/, language version 3.6) and the web-based Python interface
503 Jupyter (https://jupyter.org/index.html). Localization tables from rapi*d*STORM were
504 directly loaded and analyzed. Prior to the Python-based analysis the regions of interest
505 (ROI) were masked in the reconstructed, binned images from rapi*d*STORM using FIJI
506 (1.440, Schindelin et al., 2012). These ROIs corresponded to the terminal 6 boutons
507 according to the α-hrp staining. In earlier work on super-resolved Brp-data, density-
508 based spatial clustering of applications with noise (DBSCAN) was used to identify AZ

509 subclusters (Ehmann et al., 2014). Given the parameters k and ε, DBSCAN considers
510 a group of localizations as a cluster if there are at least k residues in a circle with radius
511 ε around a certain localization (Ester et al., 1996). Here, we used an improved
512 approach called hierarchical density-based spatial clustering of applications with noise
513 (HDBSCAN) that, in contrast, extracts the most robust clusters from a cluster hierarchy
514 over varying ε environments that are least sensible to ε variation, i.e. have the longest
515 lifetime in the cluster tree (Campello et al., 2013). The algorithm is thus more powerful
516 for cluster detection in data with variable density. We used the Python implementation
517 of HDBSCAN (McInnes et al., 2017; https://github.com/scikit-learn-contrib/hdbscan),
518 which takes 'minimum cluster size' and 'minimum samples' as the main free
519 parameters, and performed two steps of clustering with different parameters on our
520 localization data: (i) to identify the AZs, and (ii) to extract the subclusters from the AZs.
521 Setting minimum samples to smaller values than minimum cluster size allows the
522 algorithm to be less conservative, i.e. extract clusters that might be smaller than
523 minimum cluster size but very robust in the cluster hierarchy. We explored optimal
524 clustering parameters for the detection of active zones and varied minimum cluster
525 size and minimum samples in a certain range (Figure 1B, Supplementary Figure 1).
526 Too high values falsely merge adjacent AZs together (Figure 1C) whereas too low
527 values lead to fragmenting AZs into smaller clusters (Figure 1E). A wide range of
528 parameters delivered robust results and all Brp clusters in this study were extracted
529 with the combination 100 and 25 for minimum cluster size and minimum samples. A
530 second HDBSCAN on the individual AZ clusters was performed with minimum cluster
531 size 24 and minimum samples 6, and a similar number of subclusters with a
532 comparable spatial extent compared to the DBSCAN-based subcluster analysis of
533 Ehmann et al., 2014 was found (compare Figure 1H for subcluster radii and Figure 3B,
534 D for subcluster areas). For subcluster analysis, the cluster selection method was
535 changed to 'leaf' clustering, which comprises a tendency to more homogenous clusters
536 by extracting those that lie on leaf nodes of the cluster tree rather than the most stable
537 clusters. To quantify cluster area, we computed 2D alpha shapes using CGAL
538 (Computational Geometry Algorithms Library, https://www.cgal.org) in Python. The
539 geometrical concept of alpha shapes can be used to calculate the shape and thus the
540 area of a set of points. Given a finite set of points and an alpha value α, an edge of the
541 shape is drawn between two points whenever they lie on the boundary of a disk with
542 radius $\alpha^{1/2}$ that does not contain any other point (Edelsbrunner and Mücke, 1994). To

543 get the alpha shapes of the AZ clusters and AZ subclusters we choose α-values of
544 800 nm^2 and 300 nm^2, respectively. The subcluster center of mass (c.o.m.) was
545 calculated as mean of the x- and y-values of all localizations of the subcluster, and the
546 AZ c.o.m. as mean of its subcluster c.o.m.s. To estimate the distance of subcluster
547 c.o.m. from AZ c.o.m. the Euclidean distance of these points was computed. The
548 distance to the nearest subcluster c.o.m. was determined for each individual subcluster
549 c.o.m. and the mean value per AZ was obtained (Supplementary Figure 5A). To get
550 the distance between subclusters the mean subcluster radius per AZ was subtracted
551 from the subcluster center distance (Supplementary Figure 5B). For evaluation of Brp
552 cluster circularity, the ratio of the Eigenvalues of each cluster was computed, where 1
553 indicates a perfect circle and values < 1 indicate decreasing circularity (Supplementary
554 Figure 2C). Exclusion criteria for outliers in all *d*STORM data evaluations of Brp were
555 AZ area < 0.03 μm^2 (Ehmann et al., 2014) and > 0.3 μm^2, absolute localization counts
556 per AZ > 8000 and mean AZ localization density > 60000 localizations per μm^2 (about
557 3-5-fold median). Additional exclusion criteria for type Ib neuron recordings of Brp were
558 average AZ localization count < 1000 and at the same time average AZ area < 0.095
559 μm^2 per image, indicative of insufficient data quality. For visualization of the
560 localization-based results (Figure 1A, C-E, G, Figure 2A, C, Figure 3A, C, Figure 4C,
561 Supplementary Figure 3A) scatter plots were created in Python. The H function (Figure
562 1F) as derivative of Ripley's K function was computed using Python package Astropy
563 (Robitaille et al., 2013) for each individual AZ and for the random Poisson distribution.
564 Curves for display were averaged (mean ± SD). The function was evaluated in nm
565 steps for radii from 0 to 120 nm and without correction for edge effects. Simulated
566 localization data (Supplementary Figure 4) for a given radius r were created in Python
567 using the function numpy.random.uniform() passing the arguments -r and r. Thus,
568 random numbers >= -r and < r were created and used as x- and y-coordinates of
569 random points. Simulation was further constrained by computing the Euclidean
570 distance of the simulated point and the center of the simulated point cloud (x = 0, y =
571 0) and discarding all points with a distance > r. This gave rise to point clouds consisting
572 of 1500 points with circular distributions in a circle with radius r around the center. For
573 HDBSCAN analysis nine random point clouds per given radius in the same coordinate
574 system were used as input spacing the center points of adjacent point clouds three
575 radii apart. To simulate confocal resolution the point coordinates were binned into 5 nm
576 pixels. Binned images were imported as text images in FIJI and automatically

577 converted to 32-bit images were raw integrated density is equal to the absolute number
578 of localizations in a pixel. A Gaussian filter with 150 nm standard deviation (SD) was
579 applied to blur the images. The maximally possible pixel intensity after blurring was
580 0.265 arbitrary units (a. u.) corresponding to 1500 points in one pixel before blurring.
581 To achieve a somewhat realistic gain all images were equally scaled to a maximum of
582 0.35 a. u. Thresholding was performed in 8-bit with 50 a. u.
583 Confocal images were processed and evaluated in FIJI. Z-stacks were maximum
584 projected and Brp spots segmented with a pixel intensity threshold of 100 a. u. in 8-bit
585 using the 'Analyze Particles' function (Figure 4Aii). Mean pixel intensity of resulting
586 masks was measured in the original images. Corresponding Brp spots, extracted with
587 100 a. u. threshold, and Brp localization clusters were assigned manually. Only
588 clusters that were clearly distinguishable in both confocal and *d*STORM without
589 confluence to neighboring signal were used. Bouton height ranged from 0.8 to 2 µm in
590 confocal imaging. To ensure comparability to earlier quantification approaches we
591 created maximum projections of confocal data. The capture range of our *d*STORM
592 measurements is at least 1 µm, but probably even higher (Tokunaga et al., 2008). To
593 minimize bias arising from analysis of different focal planes we inspected all correlative
594 images and found no evidence for signal that was included in confocal stacks but
595 missing in *d*STORM images (compare Figure 4Ai and B). Additionally, only AZs were
596 correlated that could be clearly assigned in both imaging techniques.
597 To simulate confocal resolution (Figure 5A, B) localization tables from rapi*d*STORM
598 with 5 nm binning were converted to FIJI-readable density matrices where raw
599 integrated density corresponds to the localization count in a pixel. Images were
600 contrast enhanced to obtain 0.1 % saturated pixels, a Gaussian filter with 150 nm SD
601 was applied and the images were scaled to a pixel size of 80 nm. The same images
602 as for the localization-based analysis were included and only pixels in the same ROIs
603 as described above were used for subsequent processing and analysis. Images were
604 converted to 8-bit and the gain was adjusted by scaling all pixels in both images to the
605 same value by setting the brightest of all analyzed pixels in all images to the maximum
606 value of 255 a. u.. Following a standard protocol for the quantification of confocal data
607 of the *Drosophila* NMJ (Schmid et al., 2008; Weyhersmüller et al., 2011) a minimal
608 threshold of 50 a. u. was applied, and the 'Analyze Particles' function in FIJI was used
609 to create individual masks from the thresholded images. The resulting masks were
610 applied to the non-thresholded simulated confocal images to quantify AZ area as well

611 as the mean intensity of AZs. STED resolution in Figure 5F was simulated similarly,
612 but a Gaussian filter with 25 nm SD was applied to the density matrices. The gain of
613 all images was adjusted by setting 175 a. u. to the maximum. AZ area and mean pixel
614 intensity per AZ were measured with a threshold of 50 a. u. (Weyhersmüller et al.,
615 2011) and only Brp spots with an area > 0.03 μm^2 were analyzed. The diameter of Brp
616 spots was calculated under the assumption of a circular area. To quantify intensity
617 maxima per AZ planar-oriented, ring-like AZs were selected. Selection was performed
618 blinded with respect to the experimental groups. Single AZs were cut out from the
619 whole images. Thresholding was performed with 100 a. u. and all pixels below the
620 threshold were removed. The maxima were extracted using the 'Find Maxima' function
621 in FIJI (Prominence = 0) and quantified per AZ.
622
623 **Statistics**
624 Statistical analyses were performed with Sigma Plot 13 (Systat Software). Shapiro-
625 Wilk was used to test normality. If data were not normally distributed, we used the non-
626 parametric Mann-Whitney rank sum test for statistical analysis and reported data as
627 median (25th-75th percentile). If data were normally distributed they were reported as
628 mean ± SD unless indicated otherwise (Figure 1F). Asterisks indicate the significance
629 level (* $p < 0.05$, ** $p < 0.01$, *** $p < 0.001$) and n denotes sample number. In box plots,
630 horizontal lines represent median, boxes quartiles and whiskers 10th and 90th
631 percentiles. Scatter plots show individual data points unless indicated otherwise. Bin
632 counts in histograms were normalized to the total number of observed events which
633 was set to 1. Color codes in contour plots (Figure 1B, Supplementary Figure 1) were
634 logarithmically scaled. Linear regression curves were fitted and Spearman correlation
635 coefficient r and statistical significance p of correlations were evaluated in Sigma Plot.
636 All plots were produced with Sigma Plot software and figures assembled using Adobe
637 Illustrator (Adobe, 2015.1.1 release). Supplementary Table 1 contains all numerical
638 values not stated in text and figure legends including p-values and samples sizes.
639
640 **Code and data availability**
641 The authors declare that custom written Python code and all data sets supporting the
642 findings of this work are available from the corresponding authors.
643
644 **ACKNOWLEDGEMENTS**

This work was supported by grants from the German Research Foundation (DFG) TRR166/B06 to A.L.S. and M.H., TRR166/B02 to S.D., TRR166/B04 to M.S., KI1460/5-1 and KI1460/4-1 to R.J.K. and from the IZKF Würzburg to A.L.S. and M.H. (N229). The authors thank T. Langenhan for scientific discussions and M. Oppmann and F. Köhler for technical assistance. The authors declare no conflict of interest.

651 **REFERENCES**
652

653 1. H. L. Atwood, S. Karunanithi, Diversification of synaptic strength: presynaptic
654 elements. *Nat. Rev. Neurosci*. **3**, 497–516 (2002).
655 2. J. J. Chua, S. Kindler, J. Boyken, R. Jahn, The architecture of an excitatory
656 synapse. *J. Cell Sci.* **123**, 819–823 (2010).
657 3. R. J. Kittel, M. Heckmann, Synaptic vesicle proteins and active zone plasticity.
658 *Front. Synaptic Neurosci*. **8,** 8 (2016).
659 4. E. Neher, N. Brose, Dynamically primed synaptic vesicle states: Key to
660 understand synaptic short-term plasticity. *Neuron* **100**, 1283–1291 (2018).
661 5. G. G. Turrigiano, The self-tuning neuron: Synaptic scaling of excitatory
662 synapses. *Cell* **135**, 422–435 (2008).
663 6. G. W. Davis, M. Müller, Homeostatic control of presynaptic neurotransmitter
664 release. *Annu. Rev. Physiol.* **77**, 251–270 (2015).
665 7. G. G. Turrigiano, K. R. Leslie, N. S. Desai, L. C. Rutherford, S. B. Nelson,
666 Activity-dependent scaling of quantal amplitude in neocortical neurons. *Nature*
667 **391**, 892–896 (1998).
668 8. V. N. Murthy, T. Schikorski, C. F. Stevens, Y. Zhu, Inactivity produces increases
669 in neurotransmitter release and synapse size. *Neuron* **32**, 673–682 (2001).
670 9. T. C. Thiagarajan, M. Lindskog, R. W. Tsien, Adaptation to synaptic inactivity in
671 hippocampal neurons. *Neuron* **47**, 725–737 (2005).
672 10. M. Lindskog *et al.*, Postsynaptic GluA1 enables acute retrograde enhancement
673 of presynaptic function to coordinate adaptation to synaptic inactivity. *Proc. Natl.*
674 *Acad. Sci. U.S.A.* **107**, 21806–21811 (2010).
675 11. A. F. Jeans, F. C. van Heusden, B. Al-Mubarak, Z. Padamsey, N. J. Emptage,
676 Homeostatic presynaptic plasticity is specifically regulated by P/Q-type Ca^{2+}
677 channels at mammalian hippocampal synapses. *Cell Rep.* **21**, 341–350 (2017).
678 12. I. Delvendahl, K. Kita, M. Müller, Rapid and sustained homeostatic control of
679 presynaptic exocytosis at a central synapse. *Proc. Natl. Acad. Sci. U.S.A.* **116**,
680 23783–23789 (2019).
681 13. G. W. Davis, C. S. Goodman, Synapse-specific control of synaptic efficacy at
682 the terminals of a single neuron. *Nature* **392**, 82–86 (1998).
683 14. A. DiAntonio, S. A. Petersen, M. Heckmann, C. S. Goodman, Glutamate
684 receptor expression regulates quantal size and quantal content at the
685 Drosophila neuromuscular junction. *J. Neurosci.* **19**, 3023–3032 (1999).
686 15. C. A. Frank, M. J. Kennedy, C. P. Goold, K. W. Marek, G. W. Davis, Mechanisms
687 underlying the rapid induction and sustained expression of synaptic
688 homeostasis. *Neuron* **52**, 663–677 (2006).
689 16. M. Müller, K. S. Y. Liu, S. J. Sigrist, G. W. Davis, RIM controls homeostatic
690 plasticity through modulation of the readily-releasable vesicle pool. *J. Neurosci.*
691 **32**, 16574–16585 (2012).
692 17. M. A. Younger, M. Müller, A. Tong, E. C. Pym, G. W. Davis, A presynaptic ENaC
693 channel drives homeostatic plasticity. *Neuron* **79**, 1183–1196 (2013).
694 18. B. O. Orr, R. D. Fetter, G. W. Davis, Retrograde semaphorin-plexin signalling
695 drives homeostatic synaptic plasticity. *Nature* **550**, 109–113 (2017).
696 19. S. J. Gratz *et al.*, Endogenous tagging reveals differential regulation of Ca^{2+}
697 channels at single AZs during presynaptic homeostatic potentiation and
698 depression. *J. Neurosci.* **39**, 2416–2429 (2019).
699 20. T. C. Südhof, The presynaptic active zone. *Neuron* **75**, 11–25 (2012).

700 21. R. G. Held, C. Liu, P. S. Kaeser, ELKS controls the pool of readily releasable
701 vesicles at excitatory synapses through its N-terminal coiled-coil domains. *Elife*
702 **5**, e14862 (2016).
703 22. W. Dong *et al.*, CAST/ELKS proteins control voltage-gated Ca^{2+} channel density
704 and synaptic release probability at a mammalian central synapse. *Cell Rep.* **24**,
705 284–293 (2018).
706 23. R. J. Kittel *et al.*, Bruchpilot promotes active zone assembly, Ca^{2+} channel
707 clustering, and vesicle release. *Science* **312**, 1051–1054 (2006).
708 24. N. Ehmann *et al.*, Quantitative super-resolution imaging of Bruchpilot
709 distinguishes active zone states. *Nat. Commun.* **5**, 4650 (2014).
710 25. E. S. Peled, Z. L. Newman, E. Y. Isacoff, Evoked and spontaneous transmission
711 favored by distinct sets of synapses. *Curr. Biol.* **24**, 484–493 (2014).
712 26. M. M. Paul *et al.*, Bruchpilot and Synaptotagmin collaborate to drive rapid
713 glutamate release and active zone differentiation. *Front. Cell. Neurosci.* **9**, 29
714 (2015).
715 27. Y. Akbergenova, K. L. Cunningham, Y. V. Zhang, S. Weiss, J. T. Littleton,
716 Characterization of developmental and molecular factors underlying release
717 heterogeneity at Drosophila synapses. *Elife* **7**, e38268 (2018).
718 28. R. G. Held, P. S. Kaeser, ELKS active zone proteins as multitasking scaffolds
719 for secretion. *Open Biol.* **8**, 170258 (2018).
720 29. W. Fouquet *et al.*, Maturation of active zone assembly by Drosophila Bruchpilot.
721 *J. Cell Biol.* **186**, 129–145 (2009).
722 30. K. S. Liu *et al.*, RIM-binding protein, a central part of the active zone, is essential
723 for neurotransmitter release. *Science* **334**, 1565–1569 (2011).
724 31. S. Hallermann *et al.*, Naked dense bodies provoke depression. *J. Neurosci.* **30**,
725 14340–14345 (2010).
726 32. J. J. Sieber *et al.*, Anatomy and dynamics of a supramolecular membrane
727 protein cluster. *Science* **317**, 1072–1076 (2007).
728 33. S. Barg, M. K. Knowles, X. Chen, M. Midorikawa, W. Almers, Syntaxin clusters
729 assemble reversibly at sites of secretory granules in live cells. *Proc. Natl. Acad.*
730 *Sci. U. S. A.* **107**, 20804–20809 (2010).
731 34. G. van den Bogaart *et al.*, Membrane protein sequestering by ionic protein-lipid
732 interactions. *Nature* **479**, 552–555 (2011).
733 35. A. Weyhersmüller, S. Hallermann, N. Wagner, J. Eilers, Rapid active zone
734 remodeling during synaptic plasticity. *J. Neurosci.* **31**, 6041–6052 (2011).
735 36. P. Goel, X. Li, D. Dickman, Disparate postsynaptic induction mechanisms
736 ultimately converge to drive the retrograde enhancement of presynaptic
737 efficacy. *Cell Rep.* **21**, 2339–2347 (2017).
738 37. M. A. Böhme *et al.*, Rapid active zone remodeling consolidates presynaptic
739 potentiation. *Nat. Commun.* **10**, 1085 (2019).
740 38. M. Heilemann *et al.*, Subdiffraction-resolution fluorescence imaging with
741 conventional fluorescent probes. *Angew. Chem. Int. Ed. Engl.* **47**, 6172–6176
742 (2008).
743 39. S. van de Linde *et al.*, Direct stochastic optical reconstruction microscopy with
744 standard fluorescent probes. *Nat. Protoc.* **6**, 991–1009 (2011).
745 40. A. Löschberger *et al.*, Super-resolution imaging visualizes the eightfold
746 symmetry of gp210 proteins around the nuclear pore complex and resolves the
747 central channel with nanometer resolution. *J. Cell Sci.* **125**, 570–575 (2012).
748 41. R. J. G. B. Campello, D. Moulavi, J. Sander, "Density-based clustering based
749 on hierarchical density estimates" in *Proceedings of the 17th Pacific-Asia*

Conference on Knowledge Discovery and Data Mining, J. Pei, V. S. Tseng, L. Cao, H. Motoda, G. Xu, Eds. (Springer, 2013), pp. 160–172.

42. D. Bar-On *et al.*, Super-resolution imaging reveals the internal architecture of nano-sized syntaxin clusters. *J. Biol. Chem.* **287**, 27158–27167 (2012).
43. M. Szoboszlay, T. Kirizs, Z. Nusser, Objective quantification of nanoscale protein distributions. *Sci. Rep.* **7**, 15240 (2017).
44. T. Rahbek-Clemmensen *et al.*, Super-resolution microscopy reveals functional organization of dopamine transporters into cholesterol and neuronal activity-dependent nanodomains. *Nat. Commun.* **8**, 740 (2017).
45. N. Rebola *et al.*, Distinct nanoscale calcium channel and synaptic vesicle topographies contribute to the diversity of synaptic function. *Neuron* **104**, 693–710 (2019).
46. L. McInnes, J. Healy, S. Astels, hdbscan: Hierarchical density based clustering. *Journal of Open Source Software* **2**, 205 (2017).
47. M. A. Kiskowski, J. F. Hancock, A. K. Kenworthy, On the use of Ripley's K-function and its derivatives to analyze domain size. *Biophys. J.* **97**, 1095–1103 (2009).
48. E. S. Peled, E. Y. Isacoff, Optical quantal analysis of synaptic transmission in wild-type and rab3-mutant Drosophila motor axons. *Nat. Neurosci.* **14,** 519–526 (2011).
49. S. A. Petersen, R. D. Fetter, J. N. Noordermeer, C. S. Goodman, A. DiAntonio, Genetic analysis of glutamate receptors in Drosophila reveals a retrograde signal regulating presynaptic transmitter release. *Neuron* **19**, 1237–1248 (1997).
50. M. Nahmani, C. Lanahan, D. DeRosier, G. G. Turrigiano, High-numerical-aperture cryogenic light microscopy for increased precision of superresolution reconstructions. *Proc. Natl. Acad. Sci. U.S.A.* **114**, 3832–3836 (2017).
51. E. Neher, Vesicle pools and Ca^{2+} microdomains: New tools for understanding their roles in neurotransmitter release. *Neuron* **20**, 389–399 (1998).
52. A. H. Tang *et al.*, A trans-synaptic nanocolumn aligns neurotransmitter release to receptors. *Nature* **536**, 210–214 (2016).
53. N. Scholz *et al.*, Complexin cooperates with Bruchpilot to tether synaptic vesicles to the active zone cytomatrix. *J. Cell Biol.* **218**, 1011–1026 (2019).
54. A. K. Gillingham, S. Munro, Finding the Golgi: Golgin coiled-coil proteins show the way. *Trends Cell. Biol.* **26**, 399–408 (2016).
55. P. Y. Cheung, S. R. Pfeffer, Transport vesicle tethering at the trans Golgi network: Coiled coil proteins in action. *Front. Cell. Dev. Biol.* **4**, 18 (2016).
56. S. Karunanithi, L. Marin, K. Wong, H. L. Atwood, Quantal size and variation determined by vesicle size in normal and mutant Drosophila glutamatergic synapses. *J. Neurosci.* **22**, 10267–10276 (2002).
57. S. Takamori *et al.*, Molecular anatomy of a trafficking organelle. *Cell* **127**, 831–846 (2006).
58. D. Milovanovic, Y. Wu, X. Bian, P. De Camilli, A liquid phase of synapsin and lipid vesicles. *Science* **361**, 604–607 (2018).
59. F. Fiumara, L. Fioriti, E. R. Kandel, W. A. Hendrickson, Essential role of coiled coils for aggregation and activity of Q/N-rich prions and PolyQ proteins. *Cell* **143**, 1121–1135 (2010).
60. M. A. Böhme *et al.*, Active zone scaffolds differentially accumulate Unc13 isoforms to tune Ca^{2+} channel-vesicle coupling. *Nat. Neurosci.* **19**, 1311–1320 (2016).

61. H. Zhan, J. Bruckner, Z. Zhang, K. O'Connor-Giles, Three-dimensional imaging of Drosophila motor synapses reveals ultrastructural organizational patterns. *J. Neurogenet.* **30**, 237–246 (2016).
62. M. Tokunaga, N. Imamoto, K. Sakata-Sogawa, Highly inclined thin illumination enables clear single-molecule imaging in cells. *Nat. Methods* **5**, 159–161 (2008).
63. J. M. Ortega, Ö. Genç, G. W. Davis, Molecular mechanisms that stabilize short term synaptic plasticity during presynaptic homeostatic plasticity. *Elife* **7**, e40385 (2018).
64. C. A. Frank, T. D. James, M. Müller, Homeostatic control of Drosophila neuromuscular junction function. *Synapse* **74**, e22133 (2020).
65. L. A. Cingolani, Y. Goda, Actin in action: the interplay between the actin cytoskeleton and synaptic efficacy. *Nat. Rev. Neurosci.* **9**, 344–356 (2008).
66. B. A. Stewart, H. L. Atwood, J. J. Renger, J. Wang, C. F. Wu, Improved stability of Drosophila larval neuromuscular preparations in haemolymph-like physiological solutions. *J. Comp. Physiol. A.* **175**, 179–191 (1994).
67. S. van de Linde, M. Sauer, M. Heilemann, Subdiffraction-resolution fluorescence imaging of proteins in the mitochondrial inner membrane with photoswitchable fluorophores. *J. Struct. Biol.* **164**, 250–254 (2008).
68. S. Wolter *et al.*, Real-time computation of subdiffraction-resolution fluorescence images. *J. Microsc.* **237**, 12–22 (2010).
69. S. Wolter *et al.*, rapid*STORM: accurate, fast open-source software for localization microscopy. *Nat. Methods* **9**, 1040–1041 (2012).
70. J. Schindelin *et al.*, Fiji: an open-source platform for biological-image analysis. *Nat. Methods* **9**, 676–682 (2012).
71. U. Endesfelder, S. Malkusch, F. Fricke, M. Heilemann, A simple method to estimate the average localization precision of a single-molecule localization microscopy experiment. *Histochem. Cell Biol.* **141**, 629–638 (2014).
72. S. Malkusch, M. Heilemann, Extracting quantitative information from single-molecule super-resolution imaging data with LAMA - LocAlization Microscopy Analyzer. *Sci. Rep.* **6**, 34486 (2016).
73. M. Ester, H.-P. Kriegel, J. Sander, X. Xu, “A density-based algorithm for discovering clusters in large spatial databases with noise” in *KDD'96: Proceedings of the Second International Conference on Knowledge Discovery and Data Mining*, E. Simoudis, J. Han, U. Fayyad, Eds. (AAAI Press, 1996), pp. 226–231.
74. H. Edelsbrunner, E. P. Mücke, Three-dimensional alpha shapes. *ACM Transactions on Graphics* **13**, 43–72 (1994).
75. T. P. Robitaille *et al.*, Astropy: A community Python package for astronomy. *Astronomy and Astrophysics* **558**, A33 (2013).
76. A. Schmid *et al.*, Activity-dependent site-specific changes of glutamate receptor composition in vivo. *Nat. Neurosci.* **11**, 659–666 (2008).

842 **FIGURES**

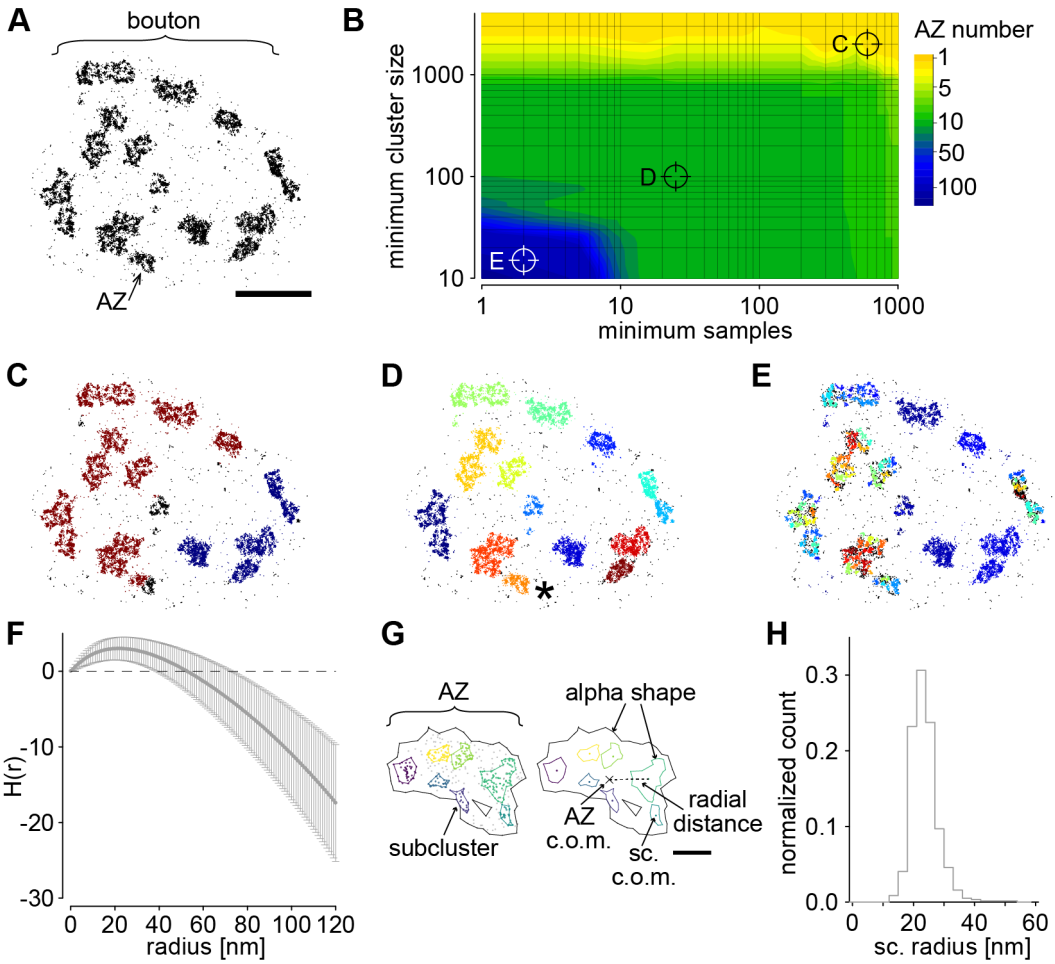

843

844 **Figure 1. Cluster analysis of presynaptic Brp localizations.**

845 (A) Scatter plot of 15470 localizations from *d*STORM of a representative type Ib bouton
846 of a wildtype *Drosophila* NMJ on abdominal muscles 6/7 stained with Brp^{Nc82} antibody
847 labelled with Alexa Fluor647 conjugated $F(ab')_2$ fragments. Arrow indicates an
848 individual cluster of Brp localizations, defined as an AZ throughout the manuscript.
849 (B) Contour plot of the number of detected AZs in the data from (A) depending on the
850 HDBSCAN clustering parameters 'minimum samples' and 'minimum cluster size'.
851 Parameter combinations for clustering in (C-E) are indicated.
852 (C-E) Data from (A) after HDBSCAN analysis. Colors indicate cluster identity,
853 unclustered localizations are displayed in black. Parameter combinations for minimum
854 cluster size and minimum samples were 2000 and 600 (C), 100 and 25 (D) and 15 and
855 2 (E). Note that multiple AZs are merged into two large clusters in (C) and that
856 individual AZs are split into multiple small clusters in (E). Minimum cluster size 100 and
857 minimum samples 25 are used for AZ detection throughout this manuscript. Asterisk
858 in (D) highlights the AZ cluster shown in (G).

859 (F) Averaged H function (grey, mean ± SD, derivative of Ripley's K function) from n =
860 568 AZs obtained from 13 NMJs from 6 wildtype animals. The maximum of the curve
861 indicates a mean subcluster (sc.) radius of 22 nm. Dashed black line indicates the
862 prediction for a random Poisson distribution.
863 (G) HDBSCAN for subcluster detection applied to an individual AZ (asterisk in D).
864 Alpha shapes used for AZ area quantification are indicated by black lines. Left: Colored
865 Brp subclusters surrounded by colored lines indicating alpha shapes. Unclustered Brp
866 localizations are shown as grey dots. Right: The centers of mass (c.o.m.) of this AZ
867 (cross) and of each subcluster (colored dots) are indicated. A dashed line shows the
868 Euclidean distance between the AZ c.o.m and an individual sc. c.o.m., referred to as
869 'radial distance'.
870 (H) Histogram of mean Brp subcluster radius per AZ assuming a circular area, median
871 (25th-75th percentile): 23 (21-26) nm) for AZs in (F). Scale bars 1 µm in (A) and 100 nm
872 in (G).
873

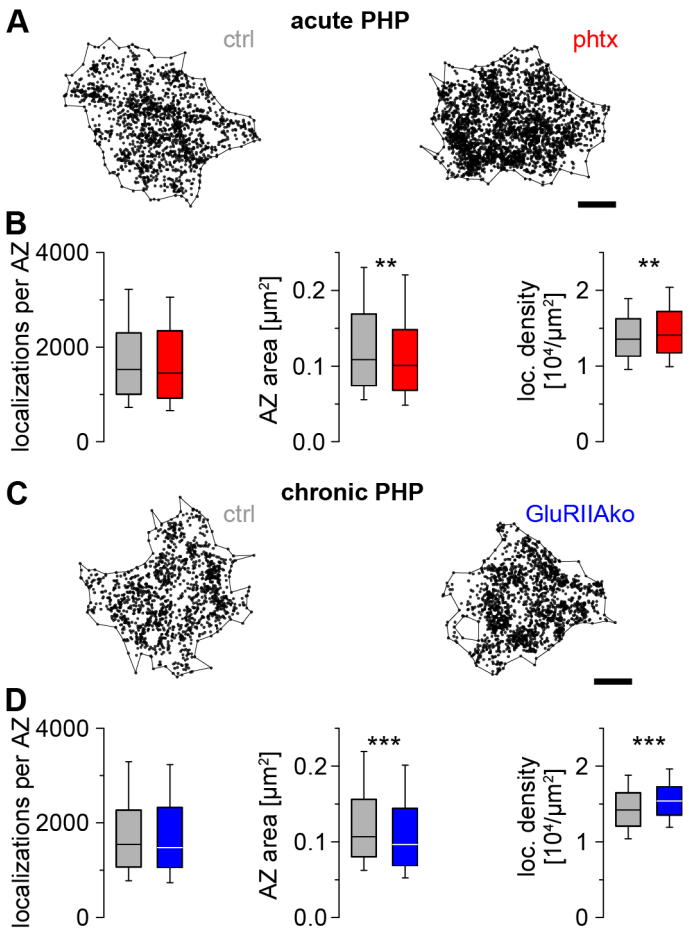

Figure 2. Acute and chronic homeostatic potentiation decrease AZ area and increase Brp density.

(A) Scatter plots of type Ib AZs from a control (ctrl, left) and a Philanthotoxin treated animal (phtx, right) for induction of acute presynaptic homeostatic potentiation (PHP). Localizations outside alpha shape are not shown for clarity.

(B) Number of Brp localizations per AZ ($p = 0.236$), AZ area ($p = 0.009$) and Brp localization density ($p = 0.009$) for ctrl (grey, n = 568 AZs from 13 NMJs from 6 animals) and phtx larvae (red, n = 792 AZs from 14 NMJs from 5 animals) shown as box plots where horizontal lines represent median, boxes quartiles and whiskers 10th and 90th percentiles. Asterisks indicate significance level (* $p < 0.05$, ** $p < 0.01$, *** $p < 0.001$).

(C) Scatter plots of type Ib AZs from a control animal (ctrl, left) and a GluRIIA receptor null mutant (GluRIIAko, right) representing chronic PHP. Localizations outside alpha shape are deleted for clarity.

(D) Number of Brp localizations per AZ ($p = 0.391$), AZ area ($p < 0.001$) and Brp localization density ($p < 0.001$) for ctrl (grey, n = 872 AZs from 19 NMJs from 6 animals) and GluRIIAko larvae (blue, n = 1020 AZs from 19 NMJs from 6 animals). Scale bars 100 nm in (A) and (C).

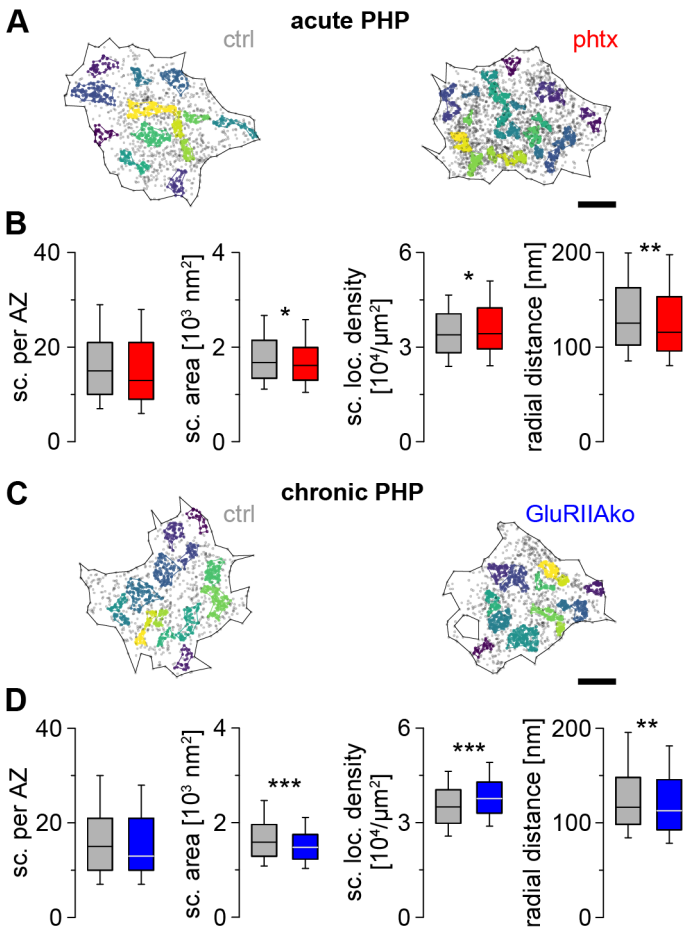

Figure 3. Homeostatic potentiation compacts AZ subclusters.

(A) Scatter plots of type Ib AZs from a ctrl and a phtx animal. Brp subclusters are colored individually, unclustered localizations are displayed as grey dots. Localizations outside alpha shape are deleted for clarity.

(B) Number of subclusters per AZ ($p = 0.084$), sc. area ($p = 0.025$), sc. localization density ($p = 0.022$) and radial distance between the AZ c.o.m. and the c.o.m. of individual subclusters ($p = 0.003$) for ctrl (grey, n = 568 AZs from 13 NMJs from 6 animals) and phtx larvae (red, n = 792 AZs from 14 NMJs from 5 animals).

(C) Scatter plots of type Ib AZs from ctrl and GluRIIAko as shown in (A).

(D) Number of subclusters per AZ ($p = 0.118$), sc. area ($p < 0.001$), sc. localization density ($p < 0.001$) and radial distance between the AZ c.o.m. and the c.o.m. of individual subclusters ($p = 0.002$) for ctrl (grey, n = 872 AZs from 19 NMJs from 6 animals) and GluRIIAko larvae (blue, n = 1020 AZs from 19 NMJs from 6 animals). Scale bars 100 nm in (A) and (C).

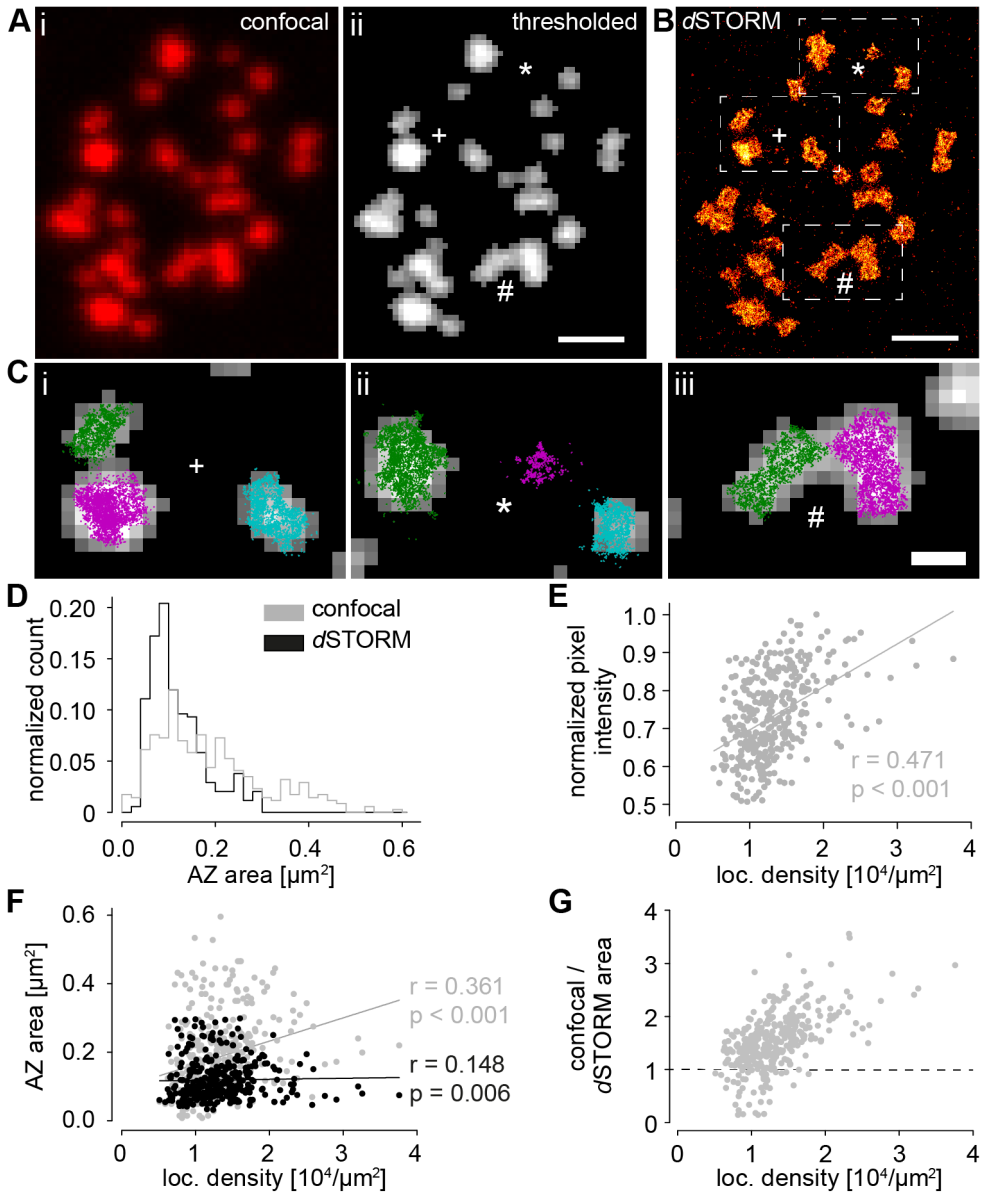

Figure 4. Correlative confocal-*d*STORM microscopy links increased localization density to increased confocal intensity and AZ area.

(A) Confocal image of a type Ib bouton. (i) unprocessed original image and (ii) after applying a 100 a. u. threshold to the original image. Symbols mark corresponding regions in (B) enlarged in (C).

(B) *d*STORM image of the same bouton as shown in (A). Boxes correspond to enlarged regions in (C).

(C) Enlarged confocal AZs thresholded at 100 a. u. in grey corresponding to boxed regions in (B) and overlaid scatter plots of Brp localizations from *d*STORM (green, magenta, blue for cluster identity). Localization clusters at the edges are not displayed. Note that the green and magenta clusters in (Ci) are not separated in confocal microscopy after thresholding, that the magenta cluster in (Cii) is lost after confocal

922 thresholding, and that the two clusters in (Ciii) are not separated by confocal
923 microscopy.
924 (D) AZ area in confocal (grey) and *d*STORM imaging (black, for D-F n = 343
925 corresponding AZs from 12 NMJs from 7 animals).
926 (E) Spearman correlation coefficient shows a positive correlation between the
927 normalized mean pixel intensity in confocal imaging and *d*STORM localization density.
928 (F) Spearman correlation coefficients show a stronger correlation between AZ area in
929 confocal imaging and localization density (grey) compared to AZ area measured with
930 *d*STORM and localization density (black).
931 (G) Ratio of confocal and *d*STORM area of corresponding AZs plotted against their
932 localization density. Values below 1 (dashed black line) indicate an underestimation of
933 confocal area quantification with respect to *d*STORM, whereas values larger than 1
934 indicate overestimation. Scale bars 1 µm in (A) and (B), 330 nm in (C).
935

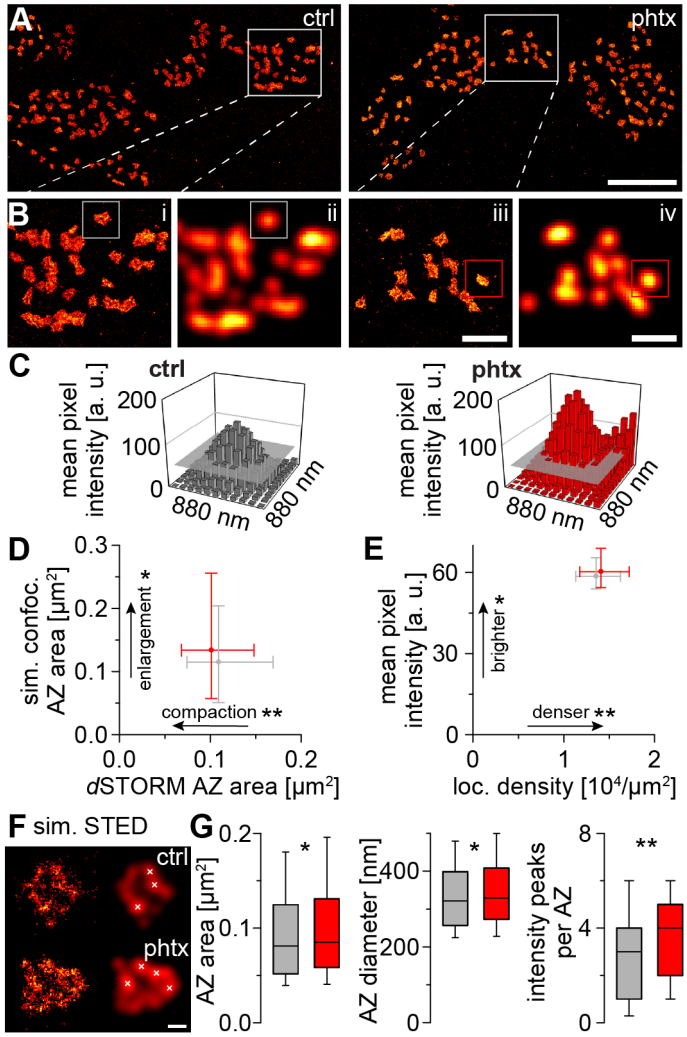

Figure 5. Compaction is reported as increased area in confocal simulation and as higher AZ diameter and more clusters in STED simulation.

(A) Sections of *d*STORM images in ctrl and phtx (5 nm binning). Boxes highlight enlarged regions in (B).

(B) Enlarged regions from (A) with *d*STORM resolution (i / iii) and simulated confocal resolution (ii / iv, 80 nm pixels, 150 nm Gaussian blur). Boxes highlight selected AZs in (C).

(C) 3D bar plots of mean pixel intensity in confocal resolution of boxed AZs in (B). Grey plane indicates thresholding level of 50 a. u. which was used for quantification in (D, E).

(D) AZ area (median (25th-75th percentile)) quantified as shown in (C), i.e. by assuming confocal resolution, plotted against AZ area from original *d*STORM analysis (data from Figure 2B) in ctrl (grey, n = 345 AZs from 13 NMJs from 6 animals in confocal resolution for (D, E)) and phtx (red, n = 457 AZs from 14 NMJs from 5 animals in confocal

resolution for (D, E), p = 0.026). Note the inverse, significant results for AZ area change.

(E) Mean pixel intensity in simulated ‘confocal’ resolution (right, p = 0.016) plotted against *d*STORM localization density (data from Figure 2B) in ctrl and phtx. Also note the inverse, significant results for this analysis.

(F) Example type Ib AZs of ctrl (upper panels) and phtx (lower panels) in *d*STORM resolution (left) and simulated STED resolution (25 nm Gaussian blur, right). White crosses indicate maxima detected with FIJI peak finding algorithm.

(G) AZ area and AZ diameter, estimated under the assumption of a circular area, obtained from simulated STED analysis in ctrl (n = 591 AZs from 13 NMJs from 6 animals) and phtx (n = 820 AZs from 14 NMJs from 5 animals, p = 0.044 and 0.044) and number of intensity peaks, i.e. Brp modules, per AZ in ctrl (n = 122 AZs from 12 NMJs from 6 animals) and phtx (n = 186 AZs from 14 NMJs from 5 animals, p = 0.002). Scale bars 4 µm in (A), 1.2 µm in (B) and 100 nm in (F).

SUPPLEMENTARY MATERIAL

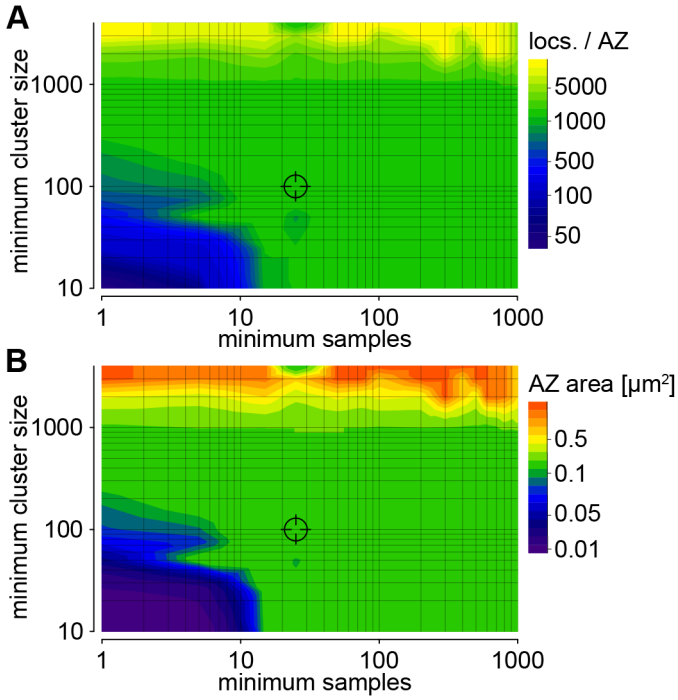

Supplementary Figure 1. Exploring HDBSCAN parameters. ***Related to Figure 1.*** Contour plots of the mean number of localizations per AZ (A) and the mean AZ area (B) for the data shown in Figure 1A depending on the HDBSCAN clustering parameters 'minimum samples' and 'minimum cluster size'. The parameter combination used for analysis throughout this study is indicated (minimum cluster size 100, minimum samples 25).

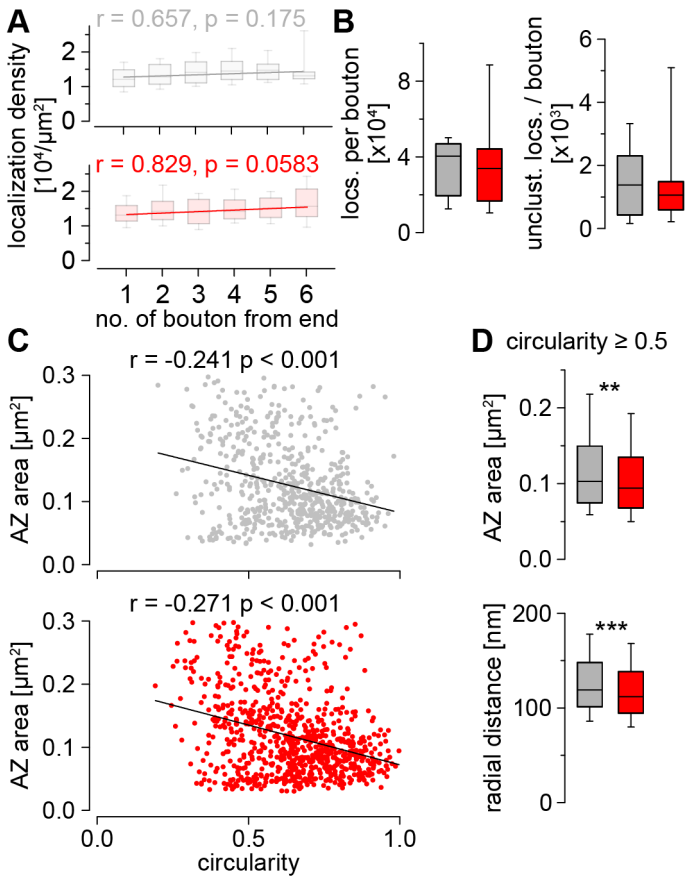

Supplementary Figure 2. Spatial differentiation, bouton analysis and circularity. ***Related to Figures 2 and 3.***

(A) Brp localization density shown as boxplots for individual boutons number 1-6 from the end of the bouton string. Spearman correlation coefficients show no significant correlation between AZ localization density and bouton position in ctrl (grey, n = 240, 140, 102, 71, 54, 19 AZs for boutons 1-6) and phtx (red, n = 251, 134, 146, 117, 78, 51 AZs for boutons 1-6, respectively).

(B) Number of all Brp localizations per bouton and number of unclustered (unclust.) localizations per bouton in ctrl (n = 13 distal Ib boutons from 6 animals) and phtx (n = 14 distal Ib boutons from 5 animals, p = 0.577 and 0.903).

(C) Scatter plots illustrating correlation of AZ circularity and area in ctrl and phtx and linear regression lines. Spearman coefficients r and p-values show negative correlations in both groups.

(D) AZs with circularity ≥ 0.5 (indicative for an AZ in top view) were used to compare AZ organization in ctrl and phtx. Box plots of AZ area and of the radial distance between the AZ c.o.m. and the c.o.m. of individual subclusters (n = 442 AZs from 13 NMJs from 6 animals and n = 621 AZs from 14 NMJs from 5 animals in ctrl and phtx, respectively, p = 0.002 and < 0.001).

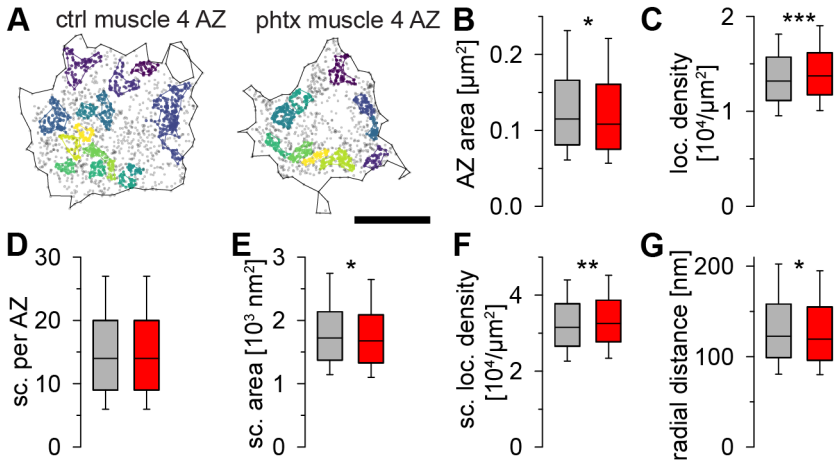

Supplementary Figure 3. AZ nanoarchitecture in type Ib boutons from NMJs on abdominal muscle 4 of *Drosophila* 3rd instar larvae. *Related to Figures 2 and 3.*

(A) Scatter plots of a ctrl and a phtx type Ib AZ on muscle 4.

(B, C) AZ area (B, $p = 0.018$) and Brp localization density (C, $p < 0.001$) in ctrl (grey, n = 1183 AZs from 20 NMJs from 6 animals for B-G) and phtx (red, n = 1445 AZs from 22 NMJs from 8 animals for B-G).

(D-G) Subcluster numbers per individual type Ib AZ (D, $p = 0.803$), subcluster area (E, $p = 0.020$), subcluster localization density (F, $p = 0.003$) and radial distance between the AZ c.o.m. and the c.o.m. of individual subclusters (G, $p = 0.022$) in both groups. Scale bar 200 nm in (A).

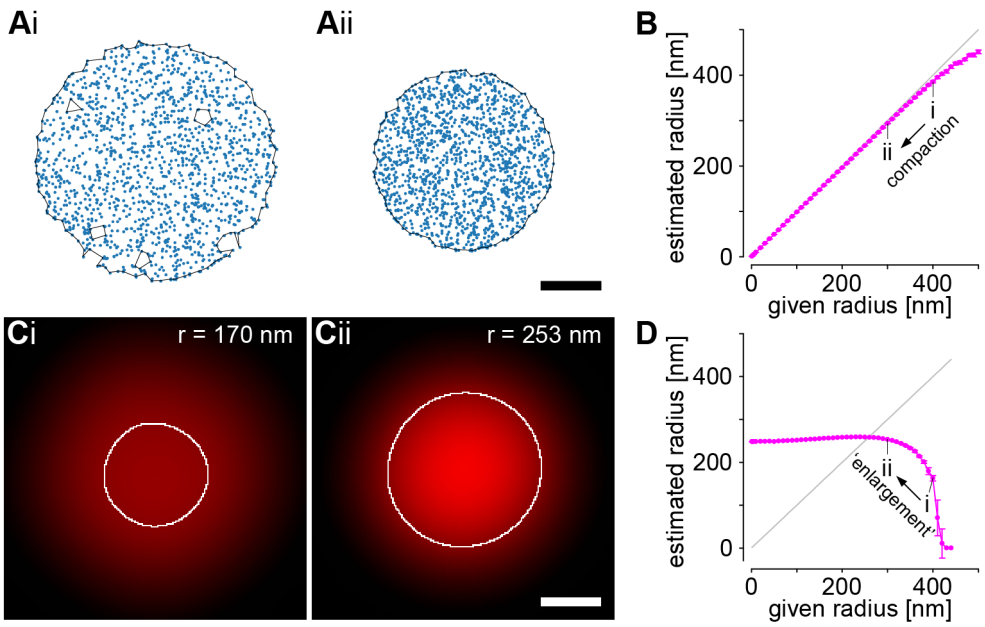

Supplementary Figure 4. Limits of area quantification.

(A) Simulation of 1500 random localizations (blue, compare ctrl value in Figure 2B, D) randomly distributed in circular areas with radius (i) 400 nm and (ii) 300 nm. Black lines indicate alpha shapes for area quantification. Holes in Ai exemplify the local failure of alpha shape-based area quantification.

(B) Radius of simulated localization clusters (magenta, mean ± SD, n = 9 simulated clusters per given radius) estimated from alpha shape area under the assumption of a circular area and line for real radius (grey, equal to given radius) plotted against the given radius for simulation. Symbols (i, ii) correspond to the given radii used in (A). This revealed a robust area quantification and allowed us to define a critical density of about 2700 localizations per μm^2 above which the estimated radius was always at least 95 % of the given radius. The first given radius below the critical density was 430 nm which exceeds the observed maximal AZ radius. We conclude that localization density is not limiting for area quantification given the high densities of AZs and of AZ subclusters in our data.

(C) Data from (A) after binning in 5 nm pixels, application of a Gaussian filter of 150 nm SD and intensity scaling to impose confocal resolution. White lines indicate a 50 a. u. threshold used for area quantification (compare standard procedures for quantification of confocal data: Schmidt et al., 2008; Weyhersmüller et al., 2011; Goel et al., 2017; Böhme et al., 2019). Radii estimated from the area under the assumption of a circular area are displayed. Strikingly, the radius measured in confocal resolution by thresholding shows an inverse effect compared to the given radii and the radii computed by alpha shapes.

1029 (D) Radii after imposing confocal resolution and thresholding on simulated localization
1030 clusters (magenta, mean ± SD, n = 10 simulated clusters per given radius) and line for
1031 real radius (grey) plotted against the given radius for simulation. Symbols (i, ii)
1032 correspond to the given radii used in (C). Note the drop of the estimated radius above
1033 a given radius of 250 nm (corresponding to a localization density roughly below 7600
1034 locs. per μm^2). This implies that the area of large objects with low molecular density
1035 (i.e. lower fluorescence intensity) is systematically underestimated by pixel- and
1036 intensity-based quantification offering an explanation for the apparent discrepancy
1037 between our data and earlier findings. Scale bars 200 nm in (A) and (C).

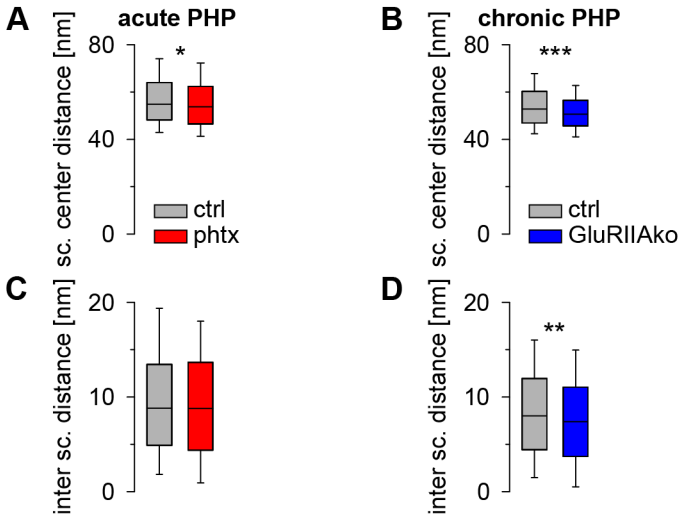

Supplementary Figure 5. Homeostatic potentiation reduces subcluster spacing. (A, B) Minimum distance between subcluster centers (mean per AZ). Sc. center distance is decreased in acute PHP (ctrl: grey, n = 568 AZs from 13 NMJs from 6 animals for (A, C); phtx: red, n = 790 AZs from 14 NMJs and 5 animals for (A, C); p = 0.024) and in chronic PHP (ctrl: grey, n = 872 AZs from 19 NMJs from 6 animals for (B, D); GluRIIAko: blue, n = 1020 AZs from 19 NMJs from 6 animals for (B, D); p < 0.001).

(C, D) Distance between subclusters (mean sc. diameter per AZ substracted from sc. center distance) in acute (C) and chronic (D) PHP. The distance between subclusters (inter sc. distance) is unchanged in acute PHP (p = 0.354) but reduced in chronic PHP (p = 0.007).

1050 **Supplementary Table 1. Data summary and statistical information.**

1051 Numerical values not stated in text and figure legends including p-values and sample
1052 sizes. Data were not normally distributed and Mann-Whitney rank sum test was used
1053 to evaluate statistical significance. The largest number stated for n indicates the
1054 sample size used for the statistical test.

1055

parameter	median (25th-75th percentile)		p-value	figure
Brp ctrl vs. phtx				
locs. per AZ	1532 (1007-2303)	1453 (926-2346) (792)	0.236	2B
AZ area [μm^2]	0.109 (0.074-0.169)	0.101 (0.068-0.148)	0.009	2B
loc. density [locs./μm^2]	13555 (11308-16236)	14082 (11756-17204)	0.009	2B
sc. per AZ	15 (10-21)	13 (9-21)	0.084	3B
locs. per sc.	57 (51-64)	56 (51-64)	0.480	
sc. area [nm^2]	1677 (1342-2149)	1617 (1301-1994)	0.025	3B
sc. loc. density [locs./μm^2]	33914 (28276-40553)	34290 (29464-42454)	0.022	3B
radial distance [nm]	125 (102-163)	116 (96-153)	0.003	3B
circularity [a.u.]	0.64 (0.52-0.75)	0.65 (0.52-0.77)	0.161	
n (AZs, NMJs, animals)	568, 13, 6	792, 14, 5		
locs. per bouton	40352 (19442-46915)	33922 (16721-44260)	0.577	S2B
unclustered locs. per bouton	1383 (428-2309)	1065 (593-1493)	0.903	S2B
n (distal Ib boutons, animals)	13, 6	14, 5		
AZ with circularity ≥ 0.5				
AZ area [μm^2]	0.103 (0.075- 0.149)	0.094 (0.068- 0.135)	0.002	S2D
radial distance [nm]	119 (101-148)	112 (95-139)	< 0.001	S2D
n (AZs, NMJs, animals)	442, 13, 6	621, 14, 5		
Brp ctrl vs. GluRIIAko				
locs. per AZ	1546 (1067-2270)	1480 (1059-2325)	0.391	2D
AZ area [μm^2]	0.107 (0.081-0.156)	0.096 (0.069-0.144)	< 0.001	2D
loc. density [locs./μm^2]	14203 (12091-16481)	15414 (13522-17294)	< 0.001	2D
sc. per AZ	15 (10-21)	13 (10-21)	0.118	3D
locs. per sc.	55 (50-62)	55 (50-62)	0.860	
sc. area [nm^2]	1588 (1291-1960)	1483 (1228-1750)	< 0.001	3D
sc. loc. density [locs./μm^2]	35053 (29821-40440)	37622 (33003-42921)	< 0.001	3D
radial distance [nm]	116 (98-148)	113 (93-146)	0.002	3D
n (AZs, NMJs, animals)	872, 19, 6	1020, 19, 6		
Brp ctrl vs. phtx muscle 4				
locs. per AZ	1591 (1022-2321)	1519 (995-2378)	0.705	
AZ area [μm^2]	0.115 (0.081-0.166)	0.108 (0.075-0.161)	0.018	S3B
loc. density [locs./μm^2]	13197 (11146-15712)	13757 (11744-16197)	< 0.001	S3C
sc. per AZ	14 (9-20)	14 (9-20)	0.803	S3D
locs. per sc.	54 (49-61)	54 (49-61)	0.834	
sc. area [nm^2]	1724 (1374-2138)	1679 (1331-2090)	0.020	S3E
sc. loc. density [locs./μm^2]	31505 (26557-37713)	32550 (27702-38679)	0.003	S3F
radial distance [nm]	123 (99-158)	119 (96-155)	0.022	S3G
n (AZs, NMJs, animals)	1183, 20, 6	1445, 22, 8		
simulated localization clusters, given radius 400 and 300 nm				

alpha shape area [µm^2]	0.463	0.270		S4A
measured radius [nm]	384	293		S4A
thresholding area [µm^2]	0.090	0.202		S4C
measured radius [nm]	170	253		S4C
correlative confocal-*d*STORM microscopy				
AZ area [µm^2]	0.164 (0.103-0.246)	0.101 (0.0768-0.147)		4D
n (AZs, NMJs, animals)	343, 12, 7			
Brp ctrl vs. phtx in confocal and STED simulation				
AZ area [µm^2]	0.115 (0.051-0.204)	0.134 (0.057-0.256)	0.026	5D
mean pixel intensity [a.u.]	58.6 (54.0-65.4)	60.3 (54.4-68.9)	0.016	5E
n (AZs, NMJs, animals)	345, 13, 6	457, 14, 5		
AZ area [µm^2]	0.081 (0.052-0.125)	0.085 (0.058-0.131)	0.044	5G
AZ diameter [nm]	322 (257-399)	329 (273-408)	0.044	5G
n (AZs, NMJs, animals)	591, 13, 6	820, 14, 5		
intensity peaks per AZ	3 (1-4)	4 (2-5)	0.002	5G
n (AZs, NMJs, animals)	122, 12, 6	186, 14, 5		
Brp subcluster distances ctrl vs. phtx				
sc. center distance [nm]	55 (48-64)	54 (47-62)	0.024	S5A
inter sc. distance [nm]	9 (5-13)	9 (4-14)	0.354	S5C
n (AZs, NMJs, animals)	568, 13, 6	790, 14, 5		
Brp subcluster distances ctrl vs. GluRIIAko				
sc. center distance [nm]	53 (47-60)	51 (46-57)	< 0.001	S5B
inter sc. distance [nm]	8 (4-12)	7 (4-11)	0.007	S5D
n (AZs, NMJs, animals)	872, 19, 6	1020, 19, 6		

1056